Defect-Assisted Hard-X-Ray Microscopy with Capillary Optics

Paweł Korecki,* Katarzyna M. Sowa, Benedykt R. Jany, and Franciszek Krok
Institute of Physics, Jagiellonian University, Łojasiewicza 11, 30-348 Kraków, Poland
(Received 21 March 2016; published 10 June 2016)

Polycapillary x-ray focusing devices are built from hundreds of thousands of bent microcapillaries that are stacked into hexagonal arrays. We show that intrinsic point defects of the optics (e.g., missing or larger capillaries) lead to the formation of multiple x-ray images of an object positioned in the focal plane. These images can be recorded in parallel, and can provide spatial resolution that is limited by the defect size and not by the focal spot size. In a proof-of-principle experiment, we demonstrate submicron resolution, which has not yet been achieved with polycapillary focusing optics. Tailored optics with a controlled distribution of "defects" could be used for multimodal nanoscale x-ray imaging with laboratory setups.

DOI: 10.1103/PhysRevLett.116.233902

For x rays, the refractive index is slightly smaller than unity [1,2], and hollow microcapillaries [3–9] or nanochannels [10,11] are capable of guiding x rays by successive total external reflections. Polycapillary x-ray focusing elements are built from hundreds of thousands of such glass microcapillaries that are stacked into hexagonal arrays [12]. They are fabricated using a repeated stack-and-draw process from fiber optics technology [13] and make it possible to concentrate or focus x rays from laboratory or synchrotron sources into intense spots. The focal spot of a polycapillary device is formed by an incoherent overlap of divergent beams from all capillaries and has a lateral diameter of $\Delta x \approx 2f\theta_c$ [12]. The focal length f, usually of few to several tens of millimeters, is determined by the bending radius of capillaries. For borosilicate glass, the critical angle for the total external reflection can be approximated as $\theta_c(\mathrm{mrad}) \approx 30/E(\mathrm{keV})$, where E is the energy of the x-ray beam. Therefore, in the hard x-ray range, the focal spot typically has a diameter between 10 and 100 μm and polycapillary "lenses" are most frequently applied in scanning micro-x-ray fluorescence (μXRF) [14–19]. Polycapillary devices are achromatic and have very large angular apertures (up to 20°). They are especially suited for collecting polychromatic radiation from a large solid angle in x-ray tube-based applications. Attached to an x-ray tube, these devices provide focal spots with sizes comparable to those of single-bounce capillaries but much more intense [20]. However, microscopy with focusing polycapillary optics has not yet reached submicron [6] or nanoresolution (<100 nm) [8], which was demonstrated in synchrotron beam experiments with single tapered capillaries and which is limited by the diameter of the capillary channel.

While polycapillary optics is not a classical imaging optics [2,9,21], the spatial resolution in both projection and scanning imaging with polycapillaries is limited by the focal spot size Δx [22,23], similar to x-ray imaging elements (i.e., for compound refractive lenses [24], focusing mirrors [25], or zone plates [26]). It was only recently demonstrated that it is possible to resolve details of an object placed inside the focal spot of a polycapillary optics [22]. Details (at a resolution of approximately 10 μm) could be decoded from a distorted image of the periodic superstructure of capillary bundles, which was treated as a coding aperture [27–29]. It was also shown that x-ray coded-aperture imaging with polycapillary optics provides depth resolution without sample or source rotation, in a way similar to classical tomography or laminography [30]. However, due to the fundamental constraints imposed by the Shannon sampling theorem [31,32], a coded-aperture approach cannot be extended for the analysis of the periodic structure of individual capillaries. In large periodic capillary arrays, structural defects are inherently present; however, in all previous reports, defects in capillary arrays were either neglected or discussed in the context of a decreased transmission and a deteriorated performance [15,33–35].

In this Letter, we demonstrate that intrinsic point defects (e.g., missing or larger capillaries), by breaking the periodicity of capillary arrays, directly lead to the formation of multiple x-ray images of an object placed inside the focal spot of a polycapillary optics. These multiple images can be analyzed in parallel, which enhances the imaging performance and provides a spatial resolution that is limited by the defect size and not by the focal spot size of the optics. In a proof-of-principle experiment, we obtained submicron resolution ($\sim$0.6 μm) that, until now, has not been reported with polycapillary focusing optics. The presented defect-assisted concept of microscopy combines the high spatial resolution provided by single capillaries with the high x-ray flux delivered by polycapillary structures, and is thereby promising in the context of multimodal nanoscale imaging with polychromatic low-brilliance laboratory x-ray sources.

The idea of defect-assisted x-ray microscopy is presented in Fig. 1. If an object is placed in the focal plane of the

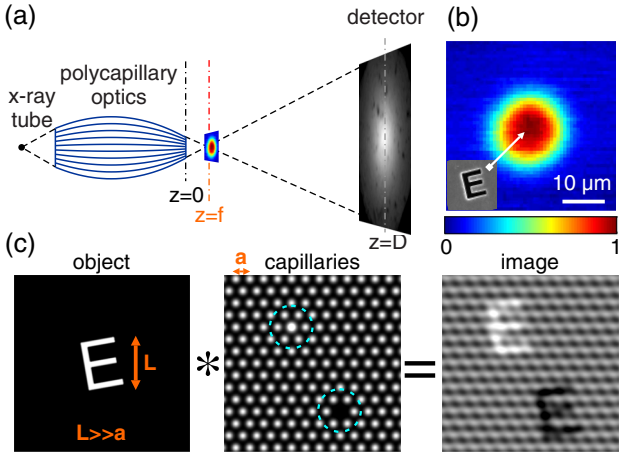

FIG. 1. Principle of defect-assisted x-ray microscopy. (a) Experimental setup. The object is placed inside the focal spot of a polycapillary focusing optics which has naturally defected capillaries. Transmitted x rays are detected using a position-sensitive detector. (b) Focal spot of the optics measured using a pinhole scan. Inset shows a SEM image of the object at the same scale. (c) Simulation of image formation. The image in the detector can be calculated as a convolution of the magnified object's transmission and the distribution of x rays from capillaries. For a perfect periodic arrangement of capillaries, information about the object is smeared. Defects (missing or larger capillaries marked with dashed circles) break the periodicity and lead to the formation of multiple x-ray images of the object.

optics, the intensity $I(\mathbf{r})$ of x rays recorded with a 2D detector can be approximated by a convolution (denoted by $*$) [35]

$$I(\mathbf{r}) = \frac{1}{S_0 M^2}[T_M(\mathbf{r})F_M(\mathbf{r})]*S_M(\mathbf{r}), \qquad (1)$$

where T_M is the transmission of the object, magnified by a factor of $(1-M)$ (see the Supplemental Material [36]), F_M describes the Gaussian-like spatial distribution of radiation in the focal spot [cf. Fig. 1(b)], at a magnification M, and S_M represents the spatial distribution of radiation at the exit plane of the optics at the same magnification. S_M is determined by the arrangement of the capillaries and their transmission properties. M is defined as $M = (f-D)/f$, where D is the detector-to-optics distance and S_0 is the total number of photons in the focal spot.

The focal spot of a polycapillary optics is always much greater than the spatial period of the capillaries. Therefore, for a periodic S_M, the convolution operation smears out the information about the object [see Fig. 1(c)]. The resulting image has the same periodicity as the capillary structure. It encodes some information about the object, but only at a set of discrete spatial frequencies that are too sparsely spaced for a well-posed object reconstruction [36]. Point defects (missing, broken, or slightly larger capillaries) change the situation, as shown by the simulation in Fig. 1(c). Such defects give rise to the formation of multiple images that are superimposed on the periodic pattern of ordered capillaries. Therefore, defect-assisted microscopy is in some ways similar to incoherent multiple-pinhole [27,42,43] or coherent multiple-reference x-ray imaging [29,44].

In order to demonstrate defect-assisted x-ray microscopy, we performed an experiment with polychromatic radiation from a tungsten anode x-ray tube (XTG5011 Apogee, Oxford Instruments) with 40-μm spot operated at 50 kV and 1 mA. The object, the letter E (6.2×4.5 μm) was milled with a focused ion beam (Dual Beam SEM/FIB Quanta 3D FEG, FEI Company) in a Au foil and was placed inside the focal spot of the optics. The optics [microlens for x-ray fluorescence spectroscopy, Institute for Scientific Instruments (IFG)] had a focal length $f \approx 2.5$ mm, an exit aperture of 1.1 mm, and produced a 11.8-μm focal spot [cf. Fig. 1(b)]. The optics consisted of approximately 3.3×10^5 capillaries arranged in 463 bundles. Transmitted x rays were recorded using a photon counting detector (Timepix, WidePIX) having 256×256 pixels with a pitch of 55 μm that was placed at a distance $D = 447$ mm from the optics. This detector covered only a small fraction (approximately 1%) of the radiation cone generated by the optics. The optics and the object were placed on piezo XYZ stages (MX35 and MS30, Mechonics). The effective energy of x rays was approximately 9 keV. For details of the experimental setup see the Supplemental Material [36].

First, for a visualization and location of defects, we placed a 0.8-μm-diameter pinhole inside the focal spot. The pinhole was milled in the same foil as the object. A pinhole approximates a pointlike object with a transmission $T_M(\mathbf{r}) = \delta(\mathbf{r})$. For such an object, Eq. (1) becomes $I(\mathbf{r}) \propto F(0)S_M(\mathbf{r})$ and the x-ray image [Fig. 2(a)] shows the magnified x-ray distribution at the exit surface of the optics. All x-ray images are presented as $I/I_0 \times \overline{I_0}$, where I and I_0 were recorded with and without the object, respectively, and $\overline{I_0}$ is the mean value of the image recorded without the object. With this data presentation, it was possible to show both the contrast and the total photon counting rates. For long exposures, final images were combined from multiple 30-s frames that were corrected for drifts by using the periodic pattern of the capillary structure as the position indicator. In Fig. 2(a), we could observe individual capillaries with a spacing of $a = 1.27 \pm 0.05$ μm and with channel diameters at the level of 1 μm. Most characteristic structural defects were marked with labels $p1 - p4$ and are shown at higher magnification in Fig. 2(b). Most frequently, defects are located at the vertices of the hexagons at the boundaries between bundles. However, they are also present in the central parts of the bundles. For example, in the areas marked with labels $p3$ and $p4$ we could observe isolated defects corresponding to broken capillaries and to capillaries with a higher transmission (most probably

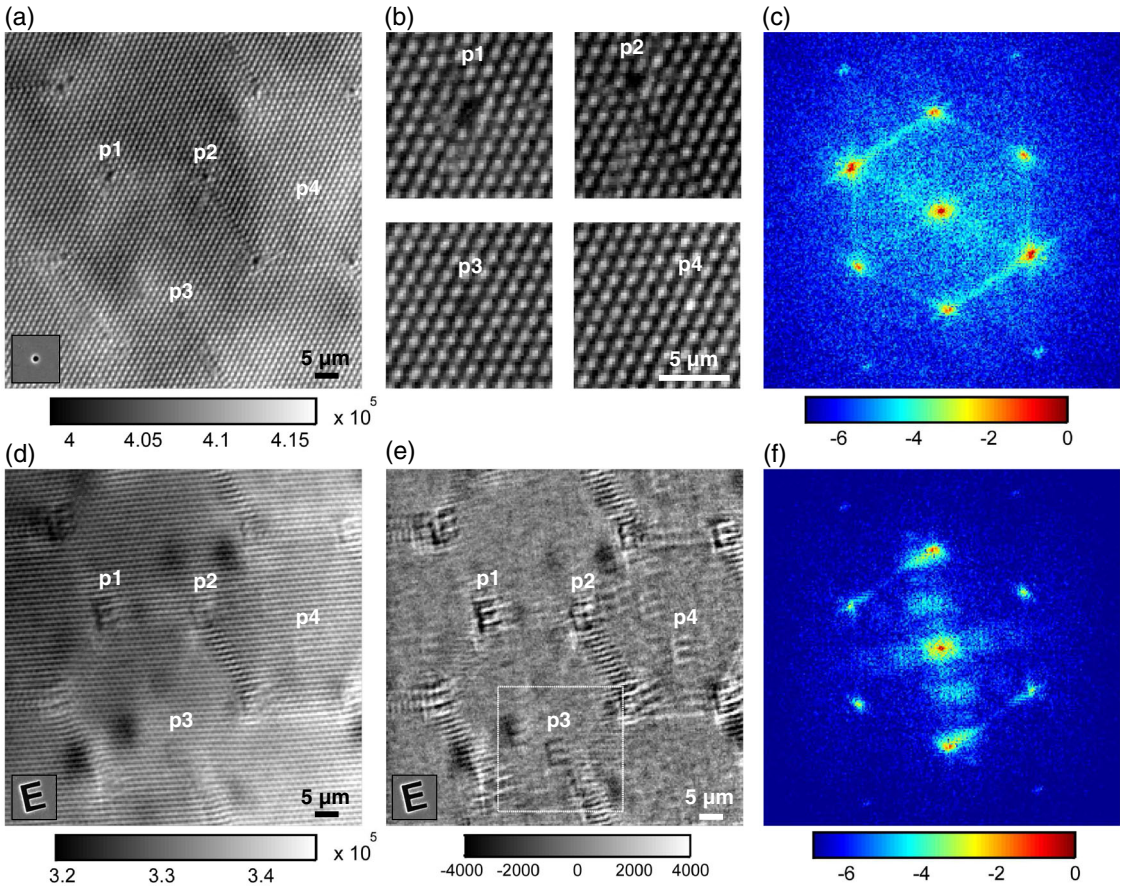

FIG. 2. Demonstration of defect-assisted x-ray microscopy. (a) Visualization of defects. An x-ray image of a small part of the optics (~1% of the total aperture) is obtained by placing a 0.8-μm-diameter pinhole inside the focal spot of the optics. (b) Zoom of typical structural defects. (c) Fourier transform of the image from (a). (d) Formation of x-ray images due to defects. The object (the letter E) is placed inside the focal spot. (e) Image from (d) after removal of the periodic component. (f) Fourier transform of image (d). Insets in bottom-left corners: SEM images of the pinhole and the object. Color bars: total number of photons recorded in each detector pixel (gray) or logarithm of Fourier transform in arbitrary units (false color scale).

having a slightly larger diameter). The low-frequency modulation of the capillary image is due to a small angular misalignment of capillaries.

After placing the object inside the focus of the optics [Fig. 2(d)], we observed the formation of distinct images of the object at locations corresponding to the positions of defects. The contrast of particular images (e.g., dark for $p3$ and white for $p4$) depends on the type of the defect. For defect complexes (e.g., $p1$ and $p2$), we could observe an overlap of multiple images. The visibility of images was enhanced in Fig. 2(e) by suppression of the periodic component using a Fourier filter.

For a parallel reconstruction [Fig. 3(a)] of the object's transmission from multiple images, we used the coded-aperture approach [22]. The object's transmission T_M was decoded by applying a Wiener deconvolution [45] to the image I from Fig. 2(e) and by using the image of capillary pattern from Fig. 2(a) as the coded aperture S_M. The signal-to-noise (SNR) parameter of the Wiener filter was frequency independent. Its optimal value was determined by maximizing SNR in the reconstruction (as the ratio of the signal power inside and outside the object area).

In order to determine the spatial resolution, we have calculated the SPSF, which is a quantitative measure of the resolution in the coded-aperture approach [28]. The SPSF is defined as the reconstructed image of a point object (in our case approximated by the pinhole); it is shown in Figs. 3(c) and 3(d). Analysis of the profiles of the SPSF indicates that the spatial resolution is at the level of 600 nm [the Nyquist frequency in Figs. 2(c) and 2(f) corresponds to a half-period spatial resolution of 310 nm]. The small side lobes of the SPSF curve result from the nonperfect suppression of the periodic signal.

The image presented in Fig. 2(d) was recorded in a 200-min exposure. Such a long exposure was used to obtain clear images formed by each individual defect and to analyze the reconstruction resolution for different types of defect complexes [36]. However, coded-aperture imaging sums up multiple images, and such long exposures

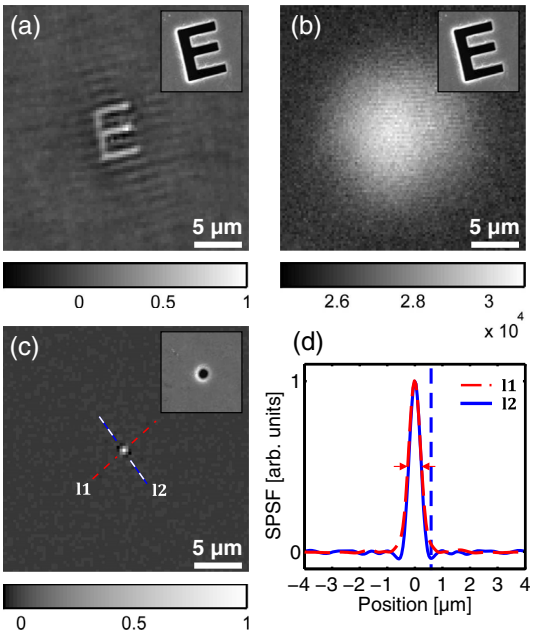

FIG. 3. Comparison of defect-assisted microscopy with standard x-ray projection imaging with the focal spot acting as a secondary source. (a) Object reconstructed using the coded aperture approach from multiple defect-assisted images (dark, low transmission; bright, high transmission). (b) X-ray image of the object positioned out of focal plane at $f + 2.5$ mm. The resolution is limited by the penumbra blur resulting from the large spot size. Color bar: photons/s/pixel. (c) System point-spread function (SPSF) of defect-assisted imaging. (d) Profiles of the SPSF interpolated from (c) along marked lines. Arrowed lines: FWHM (0.50 ± 0.15 μm) of the red dashed curve. Dashed vertical line: position of the first minimum (0.59 ± 0.15 μm) of the blue solid curve. Insets: SEM images of the object and of the 0.8-μm pinhole.

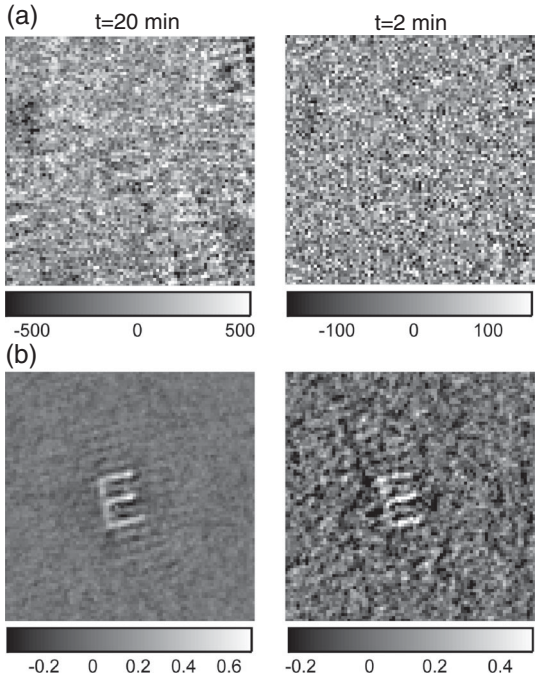

FIG. 4. Efficiency of defect-assisted x-ray microscopy. (a) X-ray images of the object for exposure times 10 and 100 times shorter than data from Fig. 2(e). Left: $t = 20$ min. Right: $t = 2$ min. Only small fragments, corresponding to the area marked with a white square in Fig. 2(e), are shown. (b) Reconstructions of the object from multiple defect-assisted images for the corresponding exposure times.

are absolutely not necessary. Figure 4 demonstrates that a high-quality reconstruction can be obtained for an exposure that is 10 times shorter. For an exposure that is 100 times shorter, the object's shape can be still recognized in the reconstruction.

To conclude, defect-assisted microscopy achieved submicron resolution, which corresponds to an order of magnitude improvement as compared to the focal-spot-limited resolution of polycapillary optics. It combines the high spatial resolution given by single capillaries with the high flux provided by polycapillary structures. Therefore, tailored devices could be used for multimodal (i.e., absorption, in-line phase contrast [46–49], and μXRF [17,18]) imaging of real samples with incoherent laboratory x-ray sources. Efficient megapixel detectors and optics "doped" with defects (solid fibers or sparse capillaries), manufactured using technology from photonic crystal fibers [50,51], would provide a massive improvement in the signal-to-noise ratio (see the Supplemental Material [36]). The spatial resolution is limited by the size of defect; hence, it is at the level of the capillary channel diameter. For a single tapered capillary, the downsizing of the channel diameter to less than 100 nm is possible [8]. It was also demonstrated that straight nanocapillary arrays are capable of transporting x rays [52], and it was recently shown that nanochannels bent to several tens of degrees can be still used to guide x-ray photons [11]. Bent nanocapillary arrays can be very fragile and contain defects; however, in this Letter, we demonstrated that the defects are very useful.

This work was financially supported by the Polish National Science Center (Grant No. DEC-2013/11/B/ST2/04057). Part of the research was carried out with equipment purchased with financial support from the European Regional Development Fund in the framework of the Polish Innovation Economy Operational Program (Contract No. POIG.02.01.00-12-023/08).

*pawel.korecki@uj.edu.pl

[1] A. H. Compton, Philos. Mag. **45**, 1121 (1923).
[2] D. Paganin, *Coherent X-Ray Optics* (Oxford University Press, New York, 2006).
[3] P. B. Hirsch and J. N. Kellar, Proc. Phys. Soc. London Sect. B **64**, 369 (1951).
[4] D. Mosher and S. J. Stephanakis, Appl. Phys. Lett. **29**, 105 (1976).

[5] A. Rindby, Nucl. Instrum. Methods Phys. Res., Sect. A **249**, 536 (1986).
[6] P. Engström, S. Larsson, A. Rindby, A. Buttkewitz, S. Garbe, G. Gaul, A. Knóchel, and F. Lechtenberg, Nucl. Instrum. Methods Phys. Res., Sect. A **302**, 547 (1991).
[7] D. J. Thiel, D. H. Bilderback, A. Lewis, and E. A. Stern, Nucl. Instrum. Methods Phys. Res., Sect. A **317**, 597 (1992).
[8] D. H. Bilderback, S. A. Hoffman, and D. J. Thiel, Science **263**, 201 (1994).
[9] D. X. Balaic and K. A. Nugent, Appl. Opt. **34**, 7263 (1995).
[10] H.-Y. Chen, S. Hoffmann, and T. Salditt, Appl. Phys. Lett. **106**, 194105 (2015).
[11] T. Salditt, S. Hoffmann, M. Vassholz, J. Haber, M. Osterhoff, and J. Hilhorst, Phys. Rev. Lett. **115**, 203902 (2015).
[12] M. Kumakhov and F. Komarov, Phys. Rep. **191**, 289 (1990).
[13] V. Beloglazov, N. Langhoff, V. Tuchin, A. Bjeoumikhov, Z. Bjeoumikhova, R. Wedel, N. Skibina, Y. S. Skibina, and M. Chainikov, J. X-Ray Sci. Technol. **13**, 179 (2005).
[14] N. Gao, I. Y. Ponomarev, Q. F. Xiao, W. M. Gibson, and D. A. Carpenter, Appl. Phys. Lett. **69**, 1529 (1996).
[15] C. A. MacDonald and W. M. Gibson, X-Ray Spectrom. **32**, 258 (2003).
[16] K. Proost, L. Vincze, K. Janssens, N. Gao, E. Bulska, M. Schreiner, and G. Falkenberg, X-Ray Spectrom. **32**, 215 (2003).
[17] L. Vincze, B. Vekemans, F. Brenker, G. Falkenberg, K. Rickers, A. Somogyi, M. Kersten, and F. Adams, Anal. Chem. **76**, 6786 (2004).
[18] B. Kanngiesser, W. Malzer, A. Rodriguez, and I. Reiche, Spectrochim. Acta B Atom. Spectros. **60**, 41 (2005).
[19] D. Hampai, S. B. Dabagov, G. Cappuccio, A. Longoni, T. Frizzi, G. Cibin, V. Guglielmotti, and M. Sala, Opt. Lett. **33**, 2743 (2008).
[20] D. Wegrzynek, R. Mroczka, A. Markowicz, E. Chinea-Cano, and S. Bamford, X-Ray Spectrom. **37**, 635 (2008).
[21] S. Hoffman, D. Thiel, and D. Bilderback, Nucl. Instrum. Methods Phys. Res., Sect. A **347**, 384 (1994).
[22] K. M. Dabrowski, D. T. Dul, and P. Korecki, Opt. Express **21**, 2920 (2013).
[23] T. Sun and C. A. MacDonald, J. Appl. Phys. **113**, 053104 (2013).
[24] A. Snigirev, V. Kohn, I. Snigireva, and B. Lengeler, Nature (London) **384**, 49 (1996).
[25] H. Mimura, S. Handa, T. Kimura, H. Yumoto, D. Yamakawa, H. Yokoyama, S. Matsuyama, K. Inagaki, K. Yamamura, Y. Sano, K. Tamasaku, Y. Nishino, M. Yabashi, T. Ishikawa, and K. Yamauchi, Nat. Phys. **6**, 122 (2010).
[26] T.-Y. Chen, Y.-T. Chen, C.-L. Wang, I. M. Kempson, W.-K. Lee, Y. S. Chu, Y. Hwu, and G. Margaritondo, Opt. Express **19**, 19919 (2011).
[27] R. H. Dicke, Astrophys. J. **153**, L101 (1968).
[28] E. E. Fenimore and T. M. Cannon, Appl. Opt. **17**, 337 (1978).
[29] S. Marchesini, S. Boutet, A. E. Sakdinawat, M. J. Bogan, S. Bajt, A. Barty, H. Chapman, M. Frank, S. P. Hau-Riege, A. Szöke *et al.*, Nat. Photonics **2**, 560 (2008).
[30] K. M. Dabrowski, D. T. Dul, A. Wrobel, and P. Korecki, Appl. Phys. Lett. **102**, 224104 (2013).
[31] D. Sayre, Acta Crystallogr. **5**, 843 (1952).
[32] K. A. Nugent, Appl. Opt. **26**, 563 (1987).
[33] T. H. K. Irving, A. G. Peele, and K. A. Nugent, Appl. Opt. **42**, 2422 (2003).
[34] A. Momose and S. Kawamoto, Jpn. J. Appl. Phys. **45**, 314 (2006).
[35] P. Korecki, T. P. Roszczynialski, and K. M. Sowa, Opt. Express **23**, 8749 (2015).
[36] See Supplemental Material at http://link.aps.org/supplemental/10.1103/PhysRevLett.116.233902, which includes Refs. [37–41], for details of the experimental setup, data analysis and SNR estimation.
[37] J. Uher, G. Harvey, and J. Jakubek, IEEE Trans. Nucl. Sci. **59**, 54 (2010).
[38] K. Ayyer *et al.*, Nature (London) **530**, 202 (2016).
[39] I. A. Cunningham and R. Shaw, J. Opt. Soc. Am. A **16**, 621 (1999).
[40] G. K. Skinner, Appl. Opt. **47**, 2739 (2008).
[41] F. Guo, X. Lin, D. Chen, S. Liu, J. He, W. Zhao, Z. Liu, and Y. Li, J. Opt. **16**, 105207 (2014).
[42] C. Brown, J. Appl. Phys. **45**, 1806 (1974).
[43] G. Groh, G. S. Hayat, and G. W. Stroke, Appl. Opt. **11**, 931 (1972).
[44] W. F. Schlotter, R. Rick, K. Chen, A. Scherz, J. Stöhr, J. Lüning, S. Eisebitt, C. Günther, W. Eberhardt, O. Hellwig, and I. McNulty, Appl. Phys. Lett. **89**, 163112 (2006).
[45] R. Willingale, M. R. Sims, and M. J. L. Turner, Nucl. Instrum. Methods Phys. Res., Sect. A **221**, 60 (1984).
[46] T. E. Gureyev, S. Mayo, S. W. Wilkins, D. Paganin, and A. W. Stevenson, Phys. Rev. Lett. **86**, 5827 (2001).
[47] M. D. de Jonge, B. Hornberger, C. Holzner, D. Legnini, D. Paterson, I. McNulty, C. Jacobsen, and S. Vogt, Phys. Rev. Lett. **100**, 163902 (2008).
[48] D. Pelliccia, A. Sorrentino, I. Bukreeva, A. Cedola, F. Scarinci, M. Ilie, A. M. Gerardino, M. Fratini, and S. Lagomarsino, Opt. Express **18**, 15998 (2010).
[49] I. Zanette, T. Zhou, A. Burvall, U. Lundström, D. H. Larsson, M. Zdora, P. Thibault, F. Pfeiffer, and H. M. Hertz, Phys. Rev. Lett. **112**, 253903 (2014).
[50] T. A. Birks, J. C. Knight, B. J. Mangan, and P. S. J. Russell, IEICE transactions on communications **E84-B**, 1211 (2001).
[51] P. Russell, Science **299**, 358 (2003).
[52] A. Bjeoumikhov, S. Bjeoumikhova, H. Riesemeier, M. Radtke, and R. Wedell, Phys. Lett. A **366**, 283 (2007).